TU Delft

Delft University of Technology

High strain rate torsional response of maraging steel parts produced by laser powder bed fusion techniques

Deformation behavior and constitutive model

Dehgahi, S.; Pirgazi, H.; Sanjari, M.; Seraj, P.; Odeshi, A.; Kestens, L.; Mohammadi, M.

DOI
10.1016/j.mechmat.2022.104296

Publication date
2022

Document Version
Final published version

Published in
Mechanics of Materials

Citation (APA)
Dehgahi, S., Pirgazi, H., Sanjari, M., Seraj, P., Odeshi, A., Kestens, L., & Mohammadi, M. (2022). High strain rate torsional response of maraging steel parts produced by laser powder bed fusion techniques: Deformation behavior and constitutive model. *Mechanics of Materials*, *168*, Article 104296. https://doi.org/10.1016/j.mechmat.2022.104296

Important note
To cite this publication, please use the final published version (if applicable).
Please check the document version above.

Copyright
Other than for strictly personal use, it is not permitted to download, forward or distribute the text or part of it, without the consent of the author(s) and/or copyright holder(s), unless the work is under an open content license such as Creative Commons.

Takedown policy
Please contact us and provide details if you believe this document breaches copyrights.
We will remove access to the work immediately and investigate your claim.

This work is downloaded from Delft University of Technology.
For technical reasons the number of authors shown on this cover page is limited to a maximum of 10.

Green Open Access added to TU Delft Institutional Repository

'You share, we take care!' - Taverne project

https://www.openaccess.nl/en/you-share-we-take-care

Otherwise as indicated in the copyright section: the publisher is the copyright holder of this work and the author uses the Dutch legislation to make this work public.

Mechanics of Materials 168 (2022) 104296

Contents lists available at ScienceDirect

Mechanics of Materials

journal homepage: www.elsevier.com/locate/mechmat

High strain rate torsional response of maraging steel parts produced by laser powder bed fusion techniques: Deformation behavior and constitutive model

S. Dehgahi [a,*], H. Pirgazi [b], M. Sanjari [a,c], P. Seraj [a], A. Odeshi [d], L. Kestens [e], M. Mohammadi [a]

[a] Marine Additive Manufacturing Centre of Excellence, University of New Brunswick, Fredericton, NB, Canada
[b] Department of Electromechanical, Systems and Metal Engineering, Ghent University, Ghent, Belgium
[c] CanmetMATERIALS, Natural Resource Canada, 183 Longwood Rd South, Hamilton, ON, Canada
[d] Department of Mechanical Engineering, University of Saskatchewan, Saskatoon, SK, Canada
[e] Materials Science and Engineering Dept, Delft University of Technology, Mekelweg 2, 2628 CD, Delft, Netherlands

ARTICLE INFO

Keywords:
Maraging steel
Laser powder bed fusion
Split Hopkinson torsion bar (SHTB)
Dynamic torsional loading
Electron backscatter diffraction

ABSTRACT

The deformation performance of maraging steel samples fabricated using the laser powder bed fusion technique was evaluated using the split Hopkinson torsion bar (SHTB) test. Thin-walled tubular maraging steel samples were deformed under dynamic torsional loading at strain rates of 260 s^{-1} to 720 s^{-1} using twist angles varying from 3 to 12°. Microstructural and textural investigations were carried out on deformed samples using the electron backscatter diffraction technique and scanning electron microscopy. Results showed that maraging steel samples fractured when deformed using an angle of twist of 12° and strain rate of 650 s^{-1}. As a result of deformation localization at high strain rates, adiabatic shear bands are developed in some thin-walled tubular torsion specimens deformed using the 12-degree angle of twist, leading to fracture. Textural studies showed that texture weakening occurred with an increment in strain rate ascribable to grain fragmentation. In this study, two models (empirically and semi-empirically) were employed for describing maraging steel performance during high strain-rate torsional loading. Simulation results based on Kobayashi-Odd and Nemat-Nasser models agreed well with the experimental data.

1. Introduction

Laser powder bed fusion (LPBF) is one of the powder-based additive manufacturing techniques that allow the fabrication of three-dimensional parts with intricate designs from a computer-aided design (CAD) model (Oliveira et al., 2020). During the LPBF process, powder metal particles are melted by a scanning laser beam and are consolidated on top of each other. Laser energy melts powders and creates solid metal upon cooling (Sing and Yeong, 2020). Additive manufacturing processes offer several prominent advantages such as reducing manufacturing time and cost, freedom of design, and capacity for fabricating complex parts. (Sing and Yeong, 2020).

Progress in laser additive manufacturing has led to the development of metal parts, including maraging steel parts with remarkable mechanical properties as opposed to their conventional counterparts (Shamsdini et al., 2020). Special attention has been paid to maraging steels ascribable to their promising properties in different applications. Maraging steel C300 (MS) is a special class of Fe–Ni alloys containing a relatively low carbon content and a martensitic phase that is reinforced with intermetallic precipitates. The high strength and high ductility of MS make it an attractive candidate for aircraft, aerospace, tool, and die-making industries (Dehgahi et al., 2020).

Recent research studies on the properties of LPBF-MS under quasi-static loading conditions have been the center of interest. The emphasis has been on laser process optimization and annealing exploration. Regarding the effect of process parameters, Souza et al. (de Souza et al., 2019) looked into the effect of part position, layer thickness, and laser speed on the mechanical performance of LPBF-MS. They reported that layer thickness plays a significant role in manufacturing time, concluding that increasing the layer thickness led to reduced manufacturing time. Regarding the effect of the annealing procedure, Conde et al. (2019) focused on the suitability of different annealing

* Corresponding author.
E-mail address: Sdehgahi@unb.ca (S. Dehgahi).

https://doi.org/10.1016/j.mechmat.2022.104296
Received 29 October 2021; Received in revised form 19 January 2022; Accepted 22 March 2022
Available online 26 March 2022
0167-6636/© 2022 Elsevier Ltd. All rights reserved.

procedures on the mechanical properties of LPBF-MS. They observed that martensite-to-austenite transformation during the aging process increases the fraction of austenite. However, the presence of the austenite phase in the matrix improves the ductility of MS parts at the expense of strength (Conde et al., 2019).

As MS parts in industries experienced high strain-rate loadings such as collision, deformation performance during high speed is important. Despite comprehensive studies on annealing procedures, process parameters, and plastic deformation during quasi-static loading conditions of LPBF-MS, mechanical performance during dynamic loading has not been studied thoroughly. However, not many research works are available on the high strain-rate compressive performance of MS produced by the LPBF technique (Dehgahi et al., 2021a) (Dehgahi et al., 2021b).

The high strain-rate performance of materials attracted much attention over the last years. The modified split Hopkinson bar technique designed by Kolsky in 1949, has been employed to study materials' dynamic deformation over the years (Kolsky, 1949). The Hopkinson bar can be used for various loading modes such as torsion, compression, and tension. Baker et al. (Baker and Yew, 1966) introduced split Hopkinson torsion bar (SHTB) for research on the dynamic torsion performance of materials. During the past years, SHTB was implemented in numerous studies to explore the dynamic torsional properties of materials (Chen et al., 2019).

In practice, MS parts tend to be employed in complex loading environments, involving a torsional mode of mechanical loading. As far as the authors can tell, there are no available reports on the high speed torsion performance of MS in the open literature. The main purpose of the research is to examine the change of the twist angle on the deformation performance of the alloy under pure torsional shear. A series of tests have been carried out on each specimen with the modified SHTB to investigate the relationship between the macroscopic stress-strain reaction of the materials with the microstructure evolution during deformation. Needless to say that numerical simulation offers an effective approach for predicting deformation performance and helps to reduce the cost and time of experimental investigations. In this study, two constitutive equations (Kobayashi-Odd and Nemat-Nasser models) were implemented with success to describe the flow performance of LPBF-MS under dynamic mechanical loading in torsion.

2. Materials and methods

2.1. Material and process parameters

Gas atomized MS powder was used for manufacturing the investigated specimens. Table 1 shows the chemical composition of the MS powder. MS powder supplied by Praxair was used to produce the printed parts via the LPBF process.

The LPBF technique was utilized for the fabrication of MS specimens in this study. Using an EOS M290 additive machine, hexagonal samples were produced. The process parameters of LPBF are given in Table 2. These parameters have been selected so that maximum density and the lowest fraction of defects could be achieved (Dehgahi et al., 2020). The strip scan strategy (rotation of laser beam about 67° after each layer deposition) was employed in this process. The LPBF process was carried out under a 99.99% argon gas atmosphere, and the bed temperature was held at 40 °C.

Table 2
Process framework of the LPBF process.

Laser power (W)	Layer thickness (μm)	Scanning speed (mm/s)	Hatch distance (μm)
285	40	960	110

2.2. High strain rate torsion test

The schematic representation of the SHTB apparatus implemented in this study is shown in Fig. 1. This apparatus is made up of a transmission bar, an incident bar, a loading wheel to twist the incident bar, and a clamp with an abrupt release mechanism. Fig. 2 shows the geometry of the test specimens, a thin-wall tube with hexagonal flanges subjected to pure shear during the rapid torsional loading. Thin-wall specimens were tested at room temperature using the angles of twist of 3, 6, 9, and 12°. In order to obtain reliable data, at least three specimens were tested for each angle of twist. The thin-wall test specimens were placed between two elastic bars. Torque is remained in the incident bar in the middle of the loading wheel and is clamped by twisting the loading wheel up to a certain angle, which is called the angle twist. The gathered torque is released by releasing the clamp instantaneously and propagates in the form of elastic waves along the incident bar. This wave (called incident wave) is captured by the strain gauge adhered to the incident bar. Some of the elastic waves are reflected on reaching the specimen. The reflected waves are captured by the strain gauge adhered to the incident bar. Some of the incident waves transmitted across the specimen rapidly twisted before propagating onto the transmitter bar as transmitted waves. The strain gauge attached to the transmitter bar captured the transmitted waves. The strain gages are located at appropriate distances from the specimen to avoid overlaying of the transmitted and incident waves. Shear strain, strain rate, and shear stress are computed from the elastic waves gained by the strain gauges adhered to the bars (Gilat and Cheng, 2000). As the incident bar should remain in the elastic region, the twist angle must be lower than 27° (Khosravifard et al., 2013). The maximum angle of twist in this experiment was 12° to avoid the bars experiencing plastic deformation.

During torsional deformation, shear stress (τ) from the measured torque (M) for any radial position and thickness can be computed through equation (1), where t is the wall thickness and r is the mean radius.

$$\tau = \frac{M}{2\pi t r^2} \tag{1}$$

The shear strain (γ) can be determined from the angle of rotation using the following equation, where L is the specimen's gage length and ϕ is the angle of rotation.

$$\gamma = \frac{\Phi r}{L} \tag{2}$$

Shear strain varies linearly with the distance from the center to the surface of a torsion specimen. Shear strain is maximum in the circumferential edge. This study focuses on the circumferential edge of the specimen.

This basic knowledge of torsion performance is employed in SHTB system for the purpose of estimating the strain-stress response of the test material at high speeds. Needles to say that in this test, the specimen experienced uniform and pure shear stress. Equations for calculating shear stress and shear strain rates from the transmitted, reflected, and incident waves are provided as follows (Majzoobi et al., 2019) (Tiwari

Table 1
Chemical composition of MS based on EOS datasheet.

Element	Mo	Ti	Co	C	Al	Ni	Fe
Composition (wt. %)	1.5–5.2	0.6–0.8	8.5–9.5	<0.03	0.05–0.15	17–19	balance

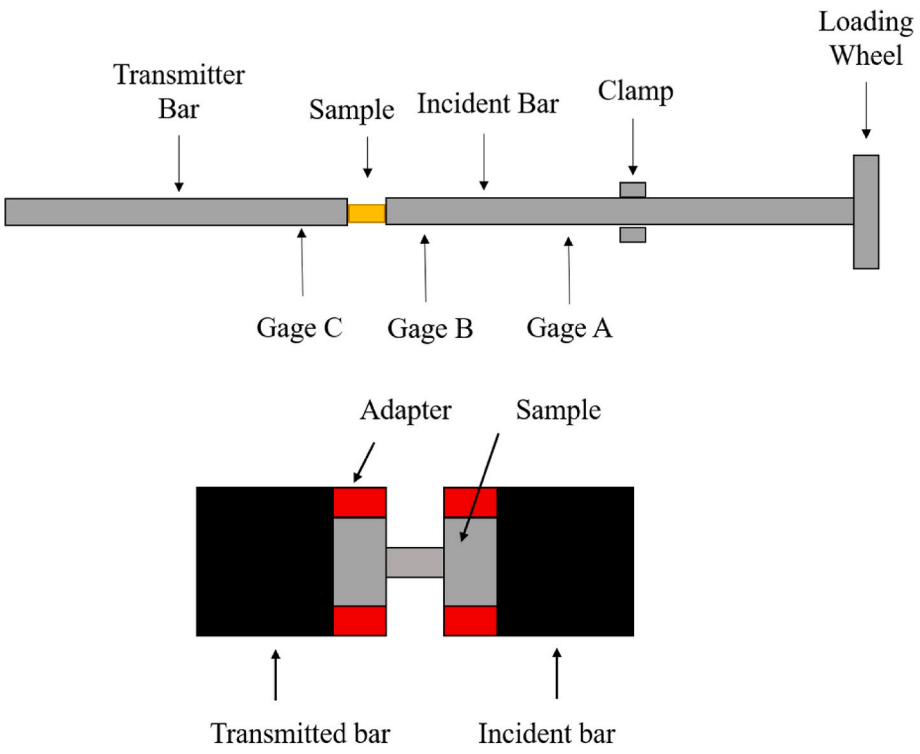

Fig. 1. Oversimplified of the torsional SHTB apparatus.

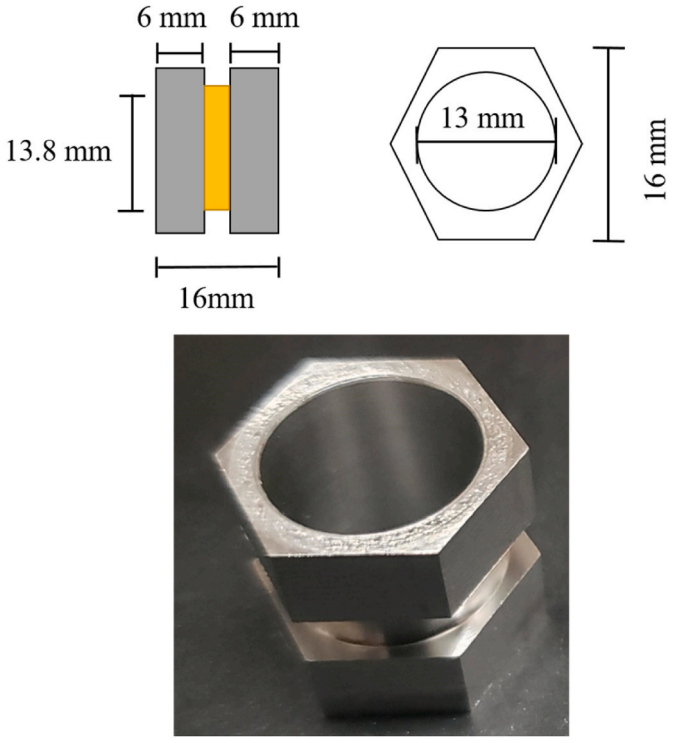

Fig. 2. The geometry of specimens in the SHTB test.

et al., 2017):

$$\dot{\gamma} = \frac{2CD_s}{L_s D}\gamma_R \tag{3}$$

$$\gamma = \frac{2CD_s}{L_s D}\int_0^t \gamma_R \, dt \tag{4}$$

$$\tau = \frac{GD^3}{8D_s^2 t_s}\gamma_T \tag{5}$$

where D_s is the average diameter of the thin wall of the specimen and C is the speed of the sound in the bar, D is the diameter of the input/output bar, L_s is specimen's gage length, t_s is the wall thickness of the specimen and G is the shear modulus of the bar material. γ (T) is transmitted strains and γ (R) is reflected strains. By using the angles of twist from 3, 6, 9 and 12°, strain rates of 260 s^{-1}, 650 s^{-1},720 s^{-1},650 s^{-1} were achieved in the specimens, respectively.

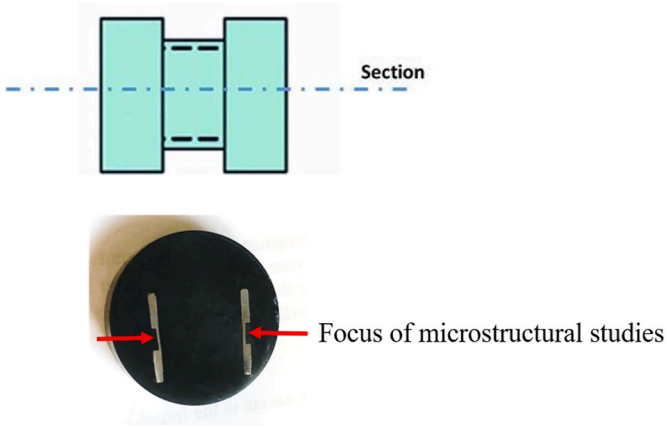

Fig. 3. Schematic and real samples used for microstructural studies.

2.3. Microstructural studies

The focus of microstructural studies was on the thin wall as shown in Fig. 3. For this purpose, samples were sectioned parallel to the axis of the specimen. Sample preparation for microscopy included polishing with SiC papers and electrochemical etching with 3% Nital solution. The microstructural inspection of twisted samples was performed using a Hitachi SU-70 Field Emission Gun (FEG) ultra-high-resolution SEM. An FEI Quanta™ 450 FEG-SEM microscope was utilized for texture measurement. With the TSL® OIM data collection software, the diffraction patterns were gathered and the OIM data analysis software was utilized for post-processing of data. Electron backscattering diffraction (EBSD) scans were performed on an area of 500 × 500 μm^2 with a step size of 500 nm to cover detailed microstructural features of the torsion samples.

3. Results and discussion

3.1. High strain rate torsion test of MS samples fabricated by LPBF

Fig. 4 shows the typical shear strain-shear strain rate curves for the specimens at different twist angles. In this study, the maximum strain rate is defined as nominal strain rate. It may be noted from Fig. 4 that strain rates first increase with strain and then decreases. In dynamic compression, it was observed that strain rates increased until they reached a plateau and then decreased (Dehgahi et al., 2021a). However, in dynamic torsion, a significant second stage (plateau) has not been observed. This shows that dynamic performance is closely attributed to the stress state. The second stage was associated with competition between thermal softening (associated with work to heat transformation) and the rate of strengthening (ascribable to strain hardening and/or strain-rate hardening). The lack of the second stage can be ascribable to the dominance of strain hardening over softening. It should be noted that in dynamic loading, at a specific strain, plastic deformation becomes inhomogeneous. This often leads to intense strain localization, which occurs when the heat generated by plastic work can not dissipate at sufficient speed, leading to an increase in temperature locally and thermal softening (Xu et al., 2008a).

Fig. 5 shows the shear strain-shear stress curves of the MS when deformed at angles of twists of 3, 6, 9 and 12°, which generate strain rates of 260 s^{-1}, 650 s^{-1}, 720 s^{-1}, and 650 s^{-1} in the specimens, respectively. The 0.2% offset yield shear strength, toughness, ultimate shear strength, strain, temperature rise, and strain rate sensitivity are summarized in Table 3. The inset shows the repeatability and reliability of the data extracted in the high speed torsion tests. The angle of twist determines the applied torsional load resulting in shear stress generated in the specimens. It is possible to see from Fig. 5 that strain rate has a

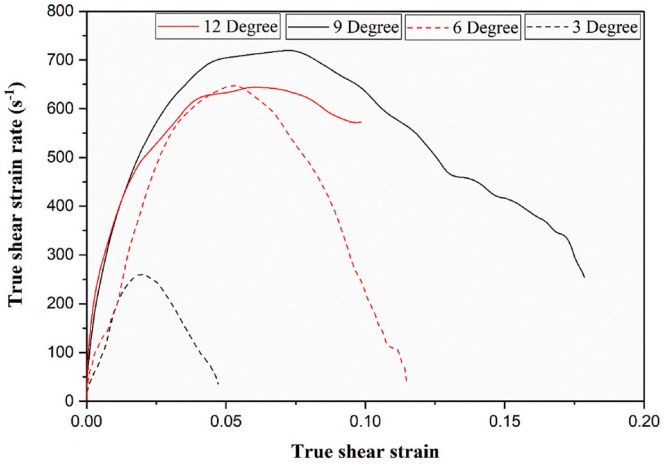

Fig. 4. True strain-strain rate curves of MS samples at different angles of twist.

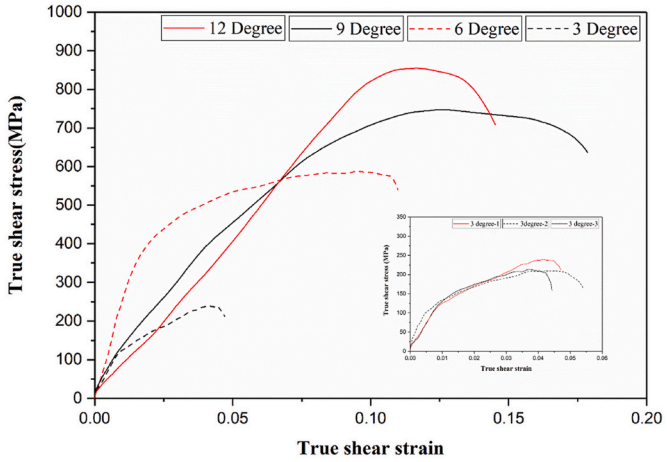

Fig. 5. Dynamic true shear strain-true shear stress curves of the MS samples at the angles of twist 3, 6, 9 and 12. The specimens' flow curves deformed at an angle of twist 3 are in the inset.

pronounced influence on ultimate stress and yield stress. The maximum shear stress with increment in the angle of twist and strain rate enhanced, which is related to strain hardening ascribable to dislocation multiplication. Maximum shear stress of 855 MPa and strain rate of 650 s^{-1} were achieved for the 12-degree angle of twist. The strain increment with an intensifying in strain rate is associated with the thermal softening phenomenon. With strain rate enhancement, more heat is generated in the sample, increasing strain. In this study, the maximum strain of 18% was achieved for the 9-degree angle of twist and strain rate of 720 s^{-1}. As the strain rate increased, high dense dislocation cells and dislocation walls formed in the microstructure to accommodate the excess strain, which results in a strength increase (Chen et al., 2019). With strain rate enhancement, the total shear strain intensified. For specimen deformed at the 12-degree angle of twist, the shear strain decreased ascribable to excessive stress concentration. Increment of shear stress, shear strain to failure with strain rate enhancement has been previously recorded for dynamic shearing of steels (Lee et al., 2004). Another interesting feature of the strain-stress curves is that all strain-stress curves have a very similar shape. As can be noted in shear stress-strain curves, shear stress increases with strain enhancement, indicating that the material is experiencing work hardening. The work-hardening rate (i.e., the slopes of the shear strain-shear stress curves in the plastic area) increases with strain rate enhancement. Indeed, work hardening is attributed to the generation of dislocations during plastic deformation (Lee et al., 2004). Flow curves show the same parabolic shape, and near the end of the test, a sudden drop in stress occurred ascribable to thermal softening. In other words, during the first stage of the deformation process, plastic strain distribution is homogenous. With continued deformation, strain distribution becomes inhomogeneous, and localized deformation likely occurred leading to fracture of the specimen. When loaded at an angle of twist of 12°, producing a strain rate of 650 s^{-1}, failure occurred in the MS samples during the dynamic torsion test.

With the angle of twist of 6 °and 12° (Fig. 5), a small plateau region can be observed, which is related to the competition of thermal softening and strain hardening. With the increase in the angle of twist to 12, thermal softening became dominant, which resulted in the failure of the specimen.

Strain rate sensitivity (SRS) is described as the dependency of strain rate hardening on strain rate, where the increment of the flow stress ascribable to strain rate enhancement can be estimated via the strain rate sensitivity parameter (α) (Niu et al., 2017). Enhancement of strain rate sensitivity with an increase in strain rate has been discussed before (Lee et al., 2004). The strain rate sensitivity of samples at different strain

Table 3
High strain rate mechanical response of the twisted MS samples fabricated by LPBF.

The angle of twist (Degree)	Strain rate (s^{-1})	Yield stress (MPa)	Maximum shear stress (MPa)	Total strain (%)	Toughness (MJ/m^3)	Temperature rise °C	Strain rate sensitivity (MPa)
3	260	189.6	239.1	4.7	7.97	1.99	143.52
6	650	389.5	587.5	10.98	53.26	13.31	198.79
9	720	581.4	747.3	17.85	99.79	24.94	252.30
12	650	767.5	854.8	11.97	58.29	14.57	231.56

rates can be computed through equation (6) where τ is the shear stress and $\dot{\gamma}$ is the shear strain rate (Niu et al., 2017).

$$\alpha = \frac{\partial \tau}{\partial (Ln\dot{\gamma})} = \frac{\tau_2 - \tau_1}{\mathrm{Ln}\left(\frac{\dot{\gamma}_2}{\dot{\gamma}_1}\right)} \tag{6}$$

At a given strain, strength increased by increasing strain rates, which means SRS improves with the enhancement of strain and strain rate. Results of strain rate sensitivity are listed in Table 3. It is possible to see that, with strain rate increment, strain rate sensitivity increased which is ascribable to increment of dislocation density (Lee et al., 2004). However, at an angle of twist of 12°, strain rate sensitivity decreases under the circumstances of intensive shear localization, which results in the dominancy of thermal softening and fracture of the sample. Shen et al. (2016) attributed negative values of strain rate sensitivity to stress concentration. With the localization of strain and thermal softening, dislocation mobility and consequently the SRS decreased. These strain rate sensitivity changes show that the changes in flow stress result from the occurrence of work hardening and thermal softening phenomena.

During dynamic deformation, ascribable to localized strain, thermomechanical instability occurred, whereby heat cannot dissipate from some regions and thermal softening occurred. The deformation temperature rise during the dynamic test can be computed through equation (7) (Tiamiyu et al., 2018) (Alaghmandfard et al., 2020):

$$\mathrm{T} - \mathrm{T0} = \Delta \mathrm{T} = \frac{\beta \mathrm{W}}{\rho.\mathrm{Cv}} \tag{7}$$

where T_0 is the temperature of the sample before the test, which is the 25 °C, and T is sample's temperature after the test. β is the Taylor-Quinney parameter and can be calculated with this equation (Tiamiyu et al., 2018) (Alaghmandfard et al., 2020):

$$\beta = \frac{\mathrm{Qp}}{\mathrm{Wp}} \tag{8}$$

$$\mathrm{Wp} = \int \tau . d\gamma \tag{9}$$

where Q is the generated heat resulted from plastic work (W_p) during high speed deformation. γ and τ are the shear strain and shear stress, respectively. MS specific heat capacity (Cv) is 450 ± 20 J/kg°C and the density (ρ) of MS is 8.2 g/cm^3. Taylor–Quinney coefficient is the efficiency of the thermomechanical conversion, which is assumed to equal 0.9, which means that 90% of plastic work converts to heat (Tiamiyu et al., 2018) (Alaghmandfard et al., 2020). The temperature rise of samples after the dynamic torsion test was estimated and is given in Table 3. Although the temperature rise is not significant, with an increase of angle of twist from 3° to 9°, the temperature increased, and decreased when the angle of twist was increased from 9 to 12°.

3.2. Microstructural studies of twisted MS samples

Fig. 6 (a) and (b) show the initial martensitic microstructure of LPBF-MS before deformation. The thin wall of the torsion samples was

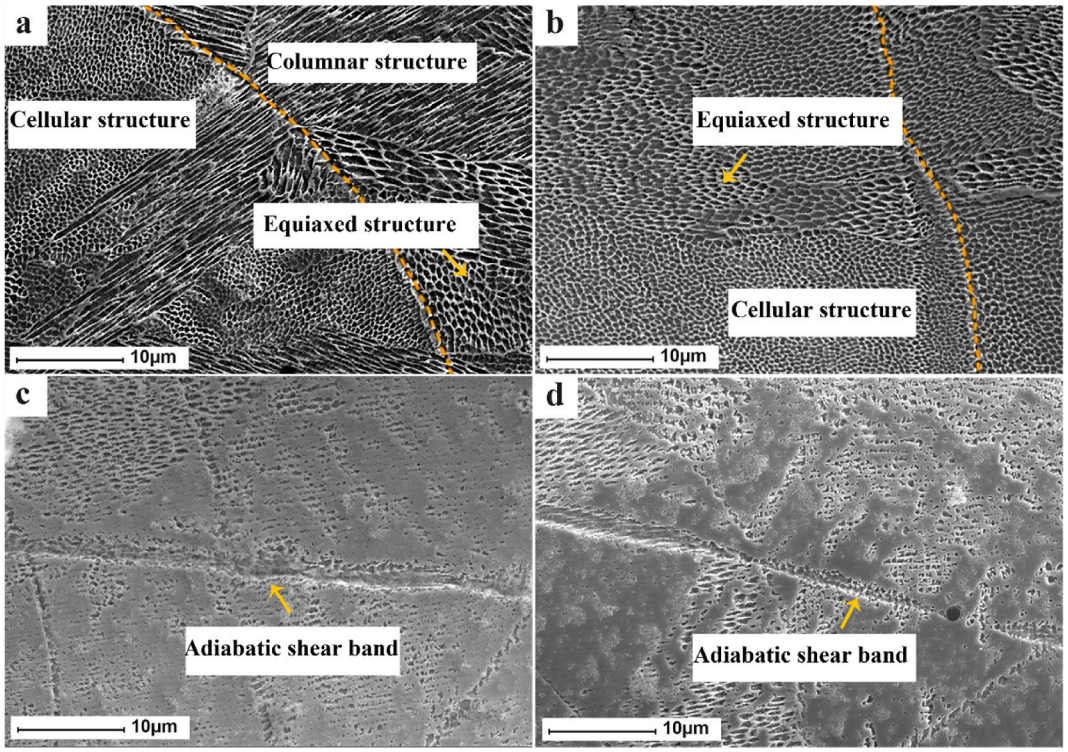

Fig. 6. Microstructures of the a) and b) MS in as-built condition, c) and d) deformed MS at strain rates of 260 s^{-1}.

investigated with SEM, as presented in Fig. 3. The microstructure of LPBF-MS in as-built condition consists of columnar, cellular, and equiaxed grains. Different morphologies can be observed in different regions of the melt pools ascribable to changes in thermal gradient and cooling rate. At the bottom of the melt pool boundaries, ascribable to a high thermal gradient, the columnar morphology starts to grow and the equiaxed grains start to form in the top central zones (Dehgahi et al., 2020) (Dehgahi et al., 2021c). Furthermore, a cellular structure can be seen between columnar grains (Dehgahi et al., 2020) (Dehgahi et al., 2021c). Fig. 6 (c) and (d) show the microstructure of loaded MS samples using an angle of twist 3° relative to a strain rate of 260 s^{-1}. Opposed to the initial as-built sample, grains undergo grain fragmentation during high speed deformation. Consequently, the unique microstructure of LPBF-MS with columnar, equiaxed, and cellular structure is destroyed.

After dynamic deformation at high speeds, a drastic change in microstructure can be observed. As deformation proceeds during dynamic loading, ascribable to localized adiabatic heating and the correlated thermal softening, loss in load-carrying capacity happened and as a result, localized shear deformation developed gradually inside the narrow bands, which are entitled adiabatic shear bands (ASBs) (Xu et al., 2008a). The advancement of localized deformation is a progressive process that occurs ascribable to localized adiabatic heating and the associated thermomechanical instability and results in ASB formation (Xu et al., 2008a). To prevent their harmful effect, it is required to understand the mechanism and conditions under which shear banding develops in the material.

It should be noted that, the geometry of the torsion sample provides inhomogeneous strain and temperature distribution and accelerates ASBs formation in the thinner region of the specimen (Duffy and Chi, 1992). Initiation and propagation of ASBs depend on stress mode, sample geometry, defects, etc. Compared to LPBF-MS deformed in compression mode (Dehgahi et al., 2021a), ASBs have observed at lower strain rates in MS deformed under dynamic torsional loading. Indeed, geometric discontinuity and stress mode accelerates inhomogeneous plastic deformation resulting in the rapid formation of ASBs. ASBs would initiate when the effective strain rate and strain reach a critical value. This critical strain rate value implies that the stress decreases ascribable to a discontinuous form of the torsion sample.

In addition, Fig. 7 (a) and (b) show the microstructure of samples deformed with an angle of twist 6° and strain rate of 650 s^{-1} and Fig. 7 (c) and (d) show the microstructure resulting from an angle of twist of 9° and strain rate of 720 s^{-1}. As can be seen, ASBs were detected in the deformed samples at angles of twist 6 and 9° in the middle of the sample (thin wall). It is worth mentioning that these ASBs developed along the shear direction (twist direction). Material inside ASBs is subjected to large strains resulting in a temperature rise, which leads to structural softening, and makes ASBs susceptible to voids and cracks formation (Xu et al., 2008a). Kobayashi et al. (Kobayashi and Dodd, 1989) proposed a model considering void nucleation and growth at a high speed torsion test. They suggested that up to the instability strain, deformation is controlled by strain hardening and thermal softening, and at the instability strain, voids form in the gauge section of the torsion specimen. These voids and cracks, which are developed inside the ASBs ascribable to shear instability lead to fracture of material at higher strain rates.

The temperature rise in Table 3 is calculated based on the total strains of the specimens. However, it is well known that the strain inside the ASBs is much higher, and as a result, the temperature inside ASBs is much more than what is calculated. Measuring the temperature inside the shear bands is extremely difficult ascribable to the short duration of initiation and propagation of the ASBs. Zhou et al. (1996) measured the shear band propagation speed of C300 MS using a high-speed camera, and they figured out that the ASBs propagation speed is about 1200 ms^{-1}. Their experiments also showed that the highest temperature of the ASBs in C300 MS is about 1400 °C (90% of its melting point). Their investigation revealed that temperature inside the ASBs is dependent on impact speed. Therefore, it can be postulated that at the higher strain rates, the evolution of shear bands occurs earlier, and propagation is faster. Besides, Guduru et al. (2001) studied the beginnings and extension of shear bands in MS. They found out that temperature distribution inside the ASBs is non-uniform. For torsion samples, the highest temperature happened in the middle of the gage section of tubular thin-walled torsion specimen where ASBs were found (Duffy and Chi,

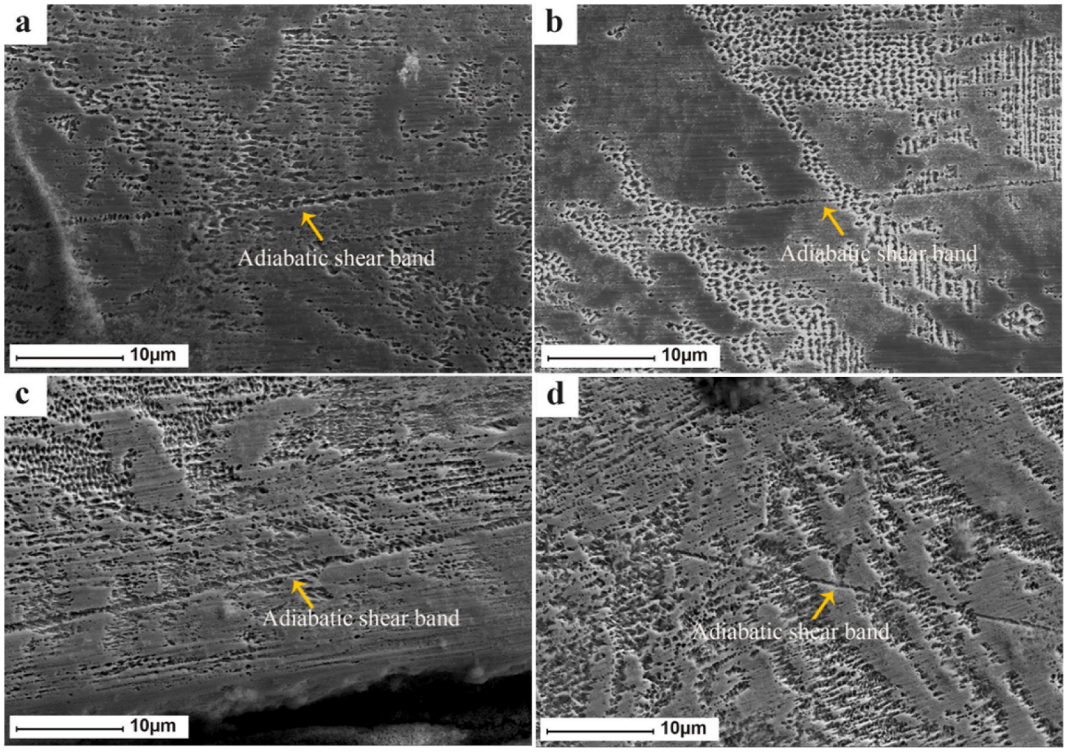

Fig. 7. Microstructures of the deformed MS samples at strain rates of a) and b) 650 s^{-1}, c) and d) 720 s^{-1}.

1992) (Kobayashi and Dodd, 1989). It should be noted that as the martensite-austenite phase conversion is diffusion-based, ascribable to lack of time in dynamic deformation, phase transformation could not occur inside ASBs (Duffy and Chi, 1992). Therefore, it can be concluded that microstructural changes ascribable to phase transformation are not involved in the final microstructure of the ASB (Duffy and Chi, 1992).

Fig. 8 shows the fracture surfaces of the MS sample loaded at the angle of twist 12° (strain rate of 650 s^{-1}) where complete separation occurs at the strain value of 12%. When the alloy was loaded at the strain rate of 650 s^{-1}, the fracture happened in the extensive localized shearing region in the middle of the sample. This type of fracture was observed before in tubular thin-walled specimens during the SHTB test (Lee et al., 2004). In the thin part of the sample, the shear strain accumulates in the middle of the specimen, which leads to fracture of torsion samples in this region. It can be noted that, the primary failure mechanism in this experiment is localized shearing. Localized shearing is an important mode of deformation, which can lead to the fracture of a sample. Under dynamic loading, ascribable to the dropping of load-carrying capacity in the adiabatically heated region, ASBs formed in the microstructure, which are susceptible regions for void and cracks formation. Nucleation, growth, and coalescence of microvoids inside ASBs occurred, which accelerates the fracture of material along the ASBs (Xu et al., 2008a). It is postulated that after an increase in temperature inside these ASBs, they cooled rapidly by surrounding bulk material and this leads to residual stress development, which results in failure (Xu et al., 2008a).

The fracture surface shows a tearing type of fracture. As shown in Fig. 8 (a), in the middle of the sample, localized shear deformation eventually led to the cleavage fracture. It can be proposed that ASBs that formed in the thin wall, encircle the specimen and led to the fracture. Because of the variation in the plasticity of ASBs and that of neighboring areas, tensile force is generated inside the ASBs (Dehgahi et al., 2021a). Ascribable to this tensile force, the opening of cracks inside the ASBs occurs, which results in the tearing of the sample. Mode III fracture (tearing mode), which propagates toward the circle leading to cleavage fracture of the torsion sample can be noted in Fig. 8 (b), (c), and (d).

3.3. Texture evolution in the LPBF-MS during dynamic torsion

Fig. 9 shows inverse pole figure (IPF-Z) maps (Z is the direction of twist) of LPBF-MS after torsion test with the angle of twist of 3, 6, and 9°, which correspond to strain rates of 260, 650, and 720 s^{-1} in the specimens, respectively. EBSD scans were conducted on the thin wall of tubular specimens, where the stress concentration of the twisted samples is maximum. Along the Z direction (shear direction), ASBs formed whereby these ASBs encircles the specimen leading to fracture of specimen deformed at the 12-degree angle of twist. It is evident from the IPF maps that crystal orientations are arranged along specific directions with enhancement of angle of twist and strain rate, and severe grain fragmentation and refinement occurred. The IPF maps at high speed show significant grain size reduction (Fig. 9 (c)). This grain refinement is also responsible for the higher shear strength of the specimen at higher strain rates based on the Hall-Petch relationship (Hadadzadeh et al., 2018a). Grain refinement is not the only mechanism for strength increment with increase of strain rate and dislocation multiplication is also involved (Dehgahi et al., 2021a). The EBSD results showed that grain size diameter for the angle of twist of 3° is 25.40 ± 3.14 μm, while that for the angle of twist of 9° is 16.18 ± 3.10 μm. For specimens deformed at an angle of twist of 9° and strain rate of 720 s^{-1}, high shear strength of 750 MPa was achieved ascribable to grain refinement. The corresponding IPF map (cf. Fig. 9(c)) shows clustering of orientations near (110) planes (green color) with the increment in strain rate. To accommodate intense shear in the thin part of the specimen, slip systems are activated. In BCC structures such as MS, slip planes are {112}, {110}, and {123} and the direction of slip is always <111> (close-packed direction) (Tian et al., 2020). In other words, slip planes such as {110} will be triggered in torsion loading mode to the accommodation of the imposed strain. It may be noted that during high speed deformation, plastic inhomogeneity causes the evolution of elongated grains across the shear direction. In Fig. 9 (c), elongated grains can be observed in the direction of the twist.

Fig. 10 shows (100) and (111) pole figures of LPBF-MS after the torsion test at the angle of twist of 3, 6, and 9° corresponding to 260,

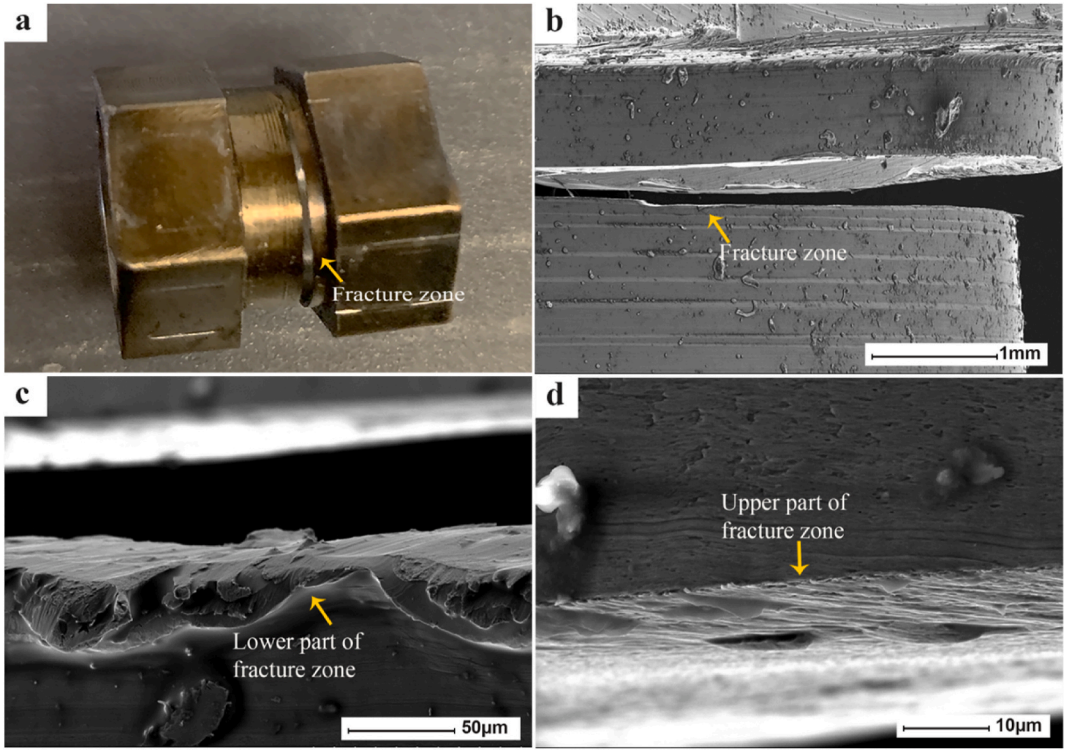

Fig. 8. Fractography of the deformed MS samples at the angle of twist of 12 and strain rates of 650 s^{-1}.

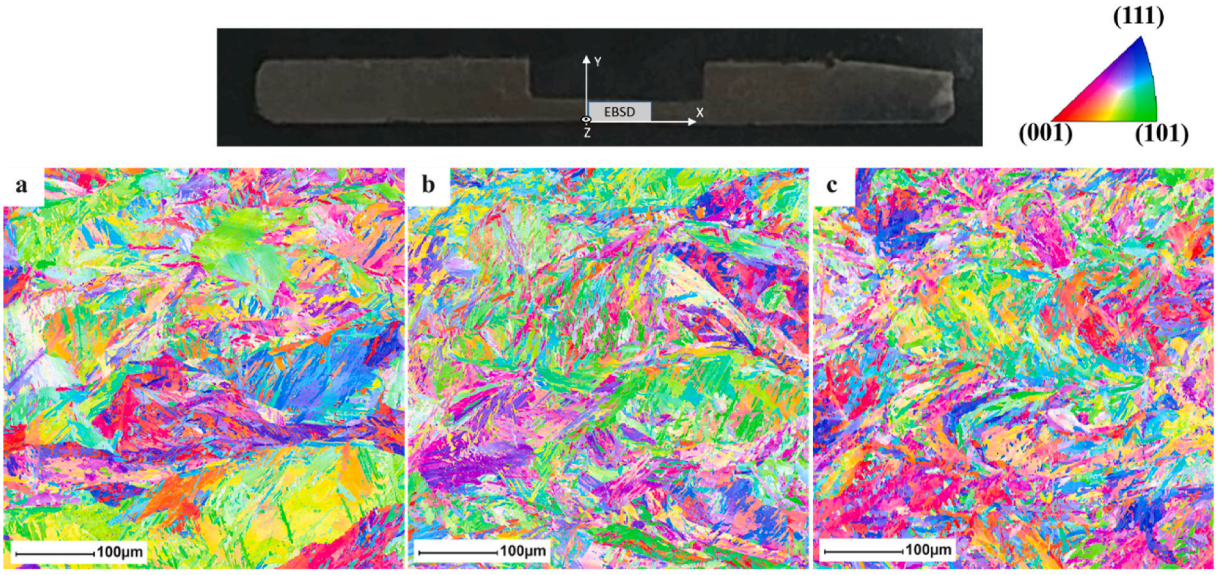

Fig. 9. IPF-Z maps of LBPF-MS samples after torsion test at the angle of twist of (a) 3, (b) 6 and (c) 9° and strain rate of a) 260, b) 650 and c) 720 s^{-1}, respectively.

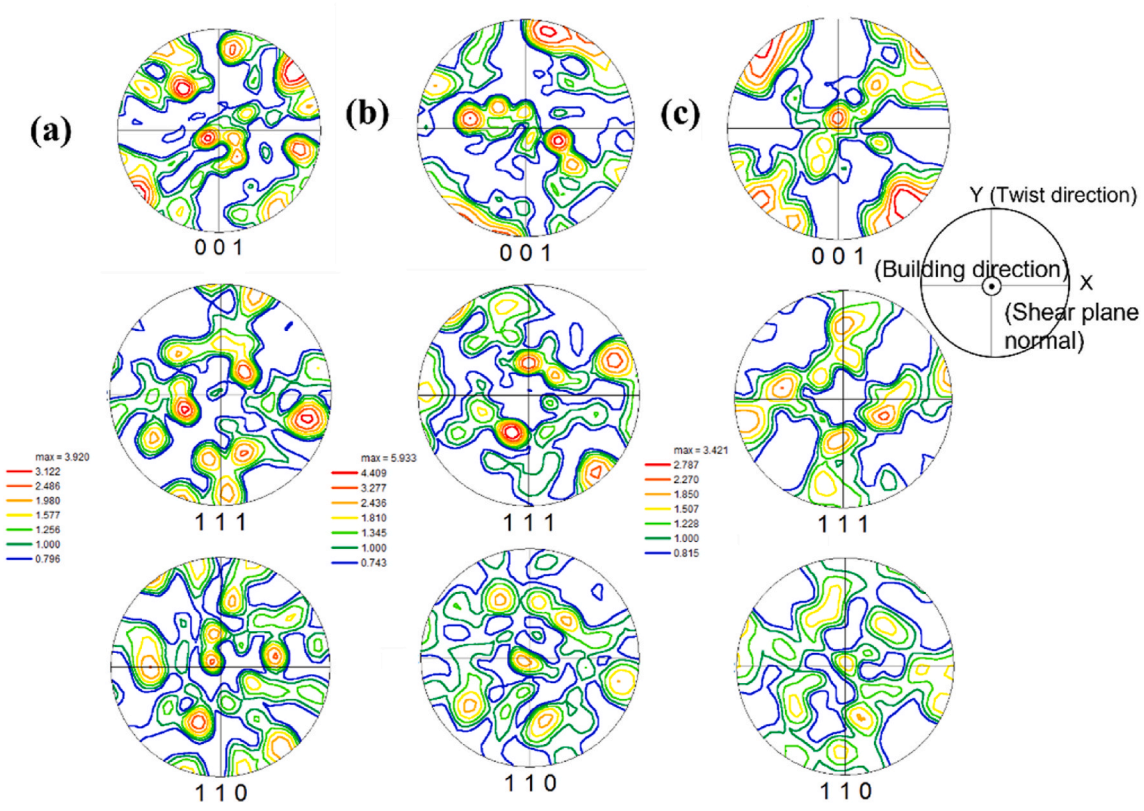

Fig. 10. (001) (110) and (111) pole figures of LBPF-MS samples after torsion test at strain rates of a) 260, b) 650 and c) 720 s^{-1}.

650, and 720 s^{-1}, strain rates respectively. As can be seen, with an increase in angle of twist and strain rate, (110) planes rotated and place along the direction of shear to accommodate plastic deformation. Torsion loading up to the strain rate of 650 s^{-1} first increases texture intensity, which then decreases with strain rate increment to 720 s^{-1}. Tiwari et al. (2017) conducted a study focusing on texture formation in an Al–Zn–Mg–Cu alloy during high speed deformation in pure shear (torsion) using SHTB. They concluded that texture weakening occurred with strain rate increment, as observed in the current study.

According to Canova et al. (1988), texture weakening shall take place for high speed compression and tension, and texture strengthening should be held for high speed shear deformation. Nevertheless, the current study (same as Tiwari's study) does not comply with Canova's.

Guaro et al. (Gurao et al., 2010) attributed the texture weakening at high speed to grain fragmentation. From the IPF map of the specimen loaded using the angle of twist of 9° and strain rate of 720 s^{-1} (Fig. 9 (c)), significant grain fragmentation occurred, which resulted in texture weakening. Guaro et al. believe that grains can not reorient completely at high speed ascribable to lack of time, resulting in grain fragmentation (Gurao et al., 2010). As deformation proceeds, dislocations are

generated, and changes in orientation within grains will occur. However, ascribable to lack of time, entire regions of grain can not orient, resulting in grain fragmentation. The true reason for fragmentation has to do with strain heterogeneities, which result from interaction processes between dislocations. These interaction processes are affected by the state of straining and hence fragmentation is more pronounced at high speeds.

Orientation distribution function (ODF) maps at $\varphi_2 = 0$ and 45° sections for the MS samples after torsion test at strain rates of 260, 650 and 720 s^{-1} are demonstrated in Fig. 11. As can be seen, the Goss component ({110}<100>) and the Brass component ({110}<112>) can be seen in the material after the high speed torsion test, which agrees well with the pole figure and IPF maps. Shen et al. (2016) associated the evolution of Goss and Brass texture with shear banding. {110}<uvw> texture was seen before in BCC structures during the torsion test (Baczynski and Jonas, 1996). As observed in SEM analysis, at high speed, ascribable to localization of strain and heat, ASBs formed in the thin wall of the twisted sample. The formation of ASBs changes the texture of the scanned area to Goss and Brass texture. Moreover, texture weakening at an angle of twist 9° and strain rate of 720 s^{-1} can be observed.

Kernel average misorientation (KAM) map of MS samples after the torsion test is presented in Fig. 12. Specifically, Fig. 12 (a), (b), and (c) show the KAM maps for specimens loaded at the angle of twist of 3, 6 and 9°, which correspond to strain rates of 260, 650 and 720 s^{-1}, respectively. In general it can be said that the KAM map is indicative of strain accumulation whereby high KAM values demonstrate deformed grains with high stored energy and high dislocation density (Hadadzadeh et al., 2018b).

It can be noted that, the KAM value for the samples deformed using 6-degree angle of twist is higher as compared to the sample with 3-degree angle of twist, which shows that dislocation density intensifies ascribable to strain hardening. However, with the increase of twist angle to 9° (720 s^{-1}), the KAM value decreased, suggesting a reduction in dislocation density. Plastic deformation of LPBF-MS at high speed

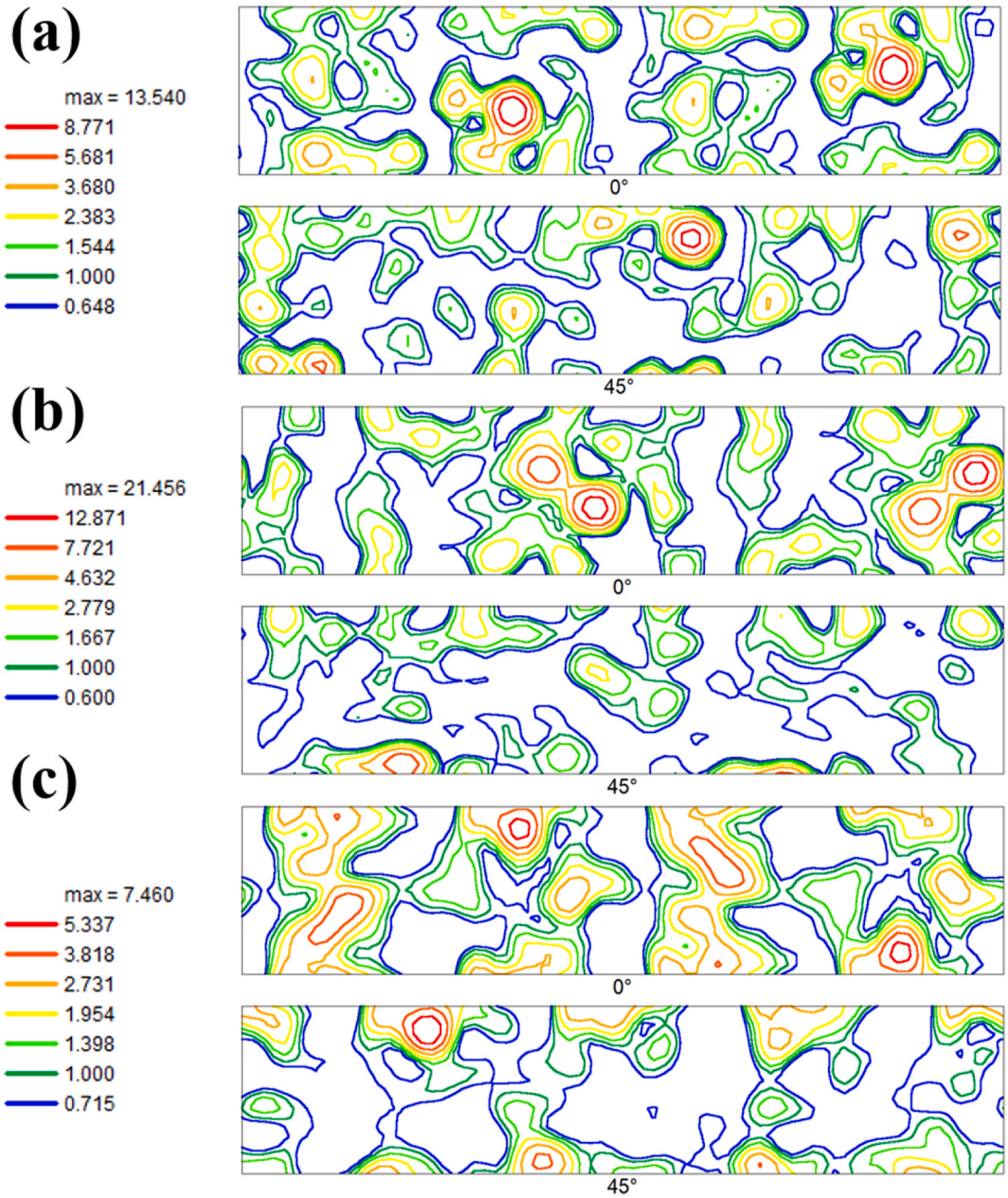

Fig. 11. The $\varphi_2 = 0°$ and 45° sections of the ODF maps of LBPF-MS samples after torsion test at strain rates of a) 260, b) 650 and c) 720 s^{-1}.

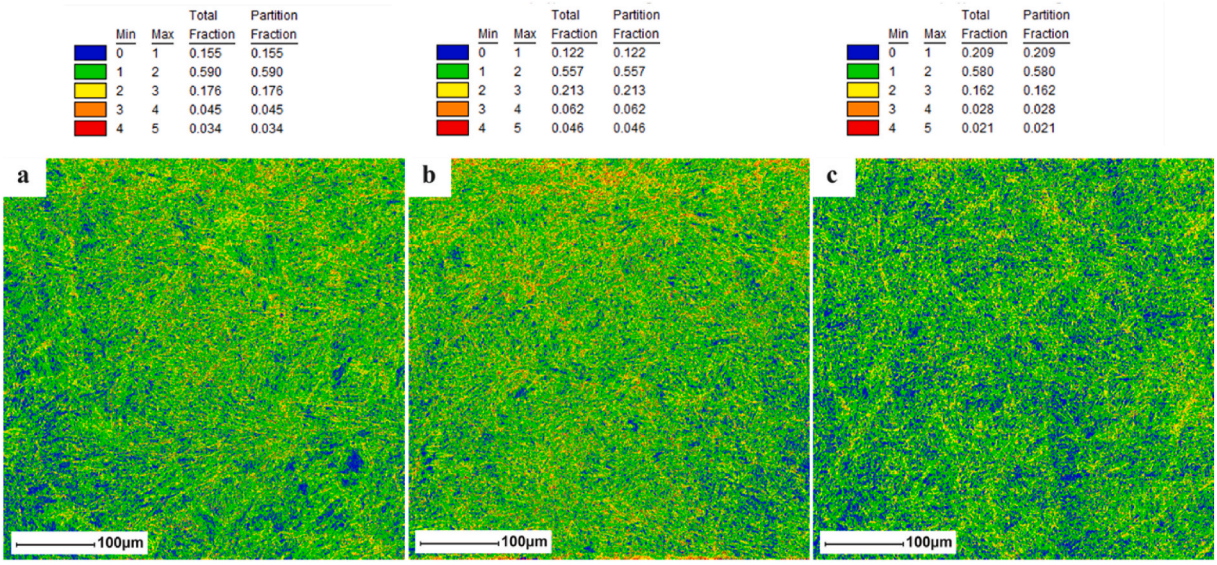

Fig. 12. KAM maps of LBPF-MS samples after torsion test at strain rates of a) 260, b) 650 and c) 720 s^{-1}.

torsion test led to the generation of new dislocations. Meanwhile, high speed causes heat generation and temperature rise as well. Temperature rise during high speed results in annihilation of dislocation dipoles and formation of dislocation free subgrains (Hadadzadeh et al., 2018b). This means that for the angle of twist of 3–6°, strain hardening has dominated over recovery.

Moreover, increasing the angle of twist to 9°, increases the amount of heat generated in the alloy and therefore, the formation of dislocation-free subgrains will occur more readily. In other words, thermal softening becomes more prominent for the angle of twist of 9° resulting in dislocation annihilation. This change in KAM values suggests that restoration processes such as dynamic recovery occurs when the alloy is deformed using the twist angle of 9°. Dynamic recovery consists of dislocations movement, resulting in subgrains and low-angle grain boundaries (Tiwari et al., 2017). Furthermore, for the angle of twist 9°, the number fraction of KAM values < 1 has increased, which confirms the development of dynamic recrystallization (Tiwari et al., 2017) (Hadadzadeh et al., 2018b). With the increase of twist angle from 3 to 6°, the dislocation density increased and the driving force for recovery processes also increased. Activation of dynamic recrystallization processes occurred for deformation 9-degree angle of twist. ASBs are regions of localized deformation, and recrystallized grains in ASBs have been reported by other researchers (Xu et al., 2008b). Xu et al. (2008b) proposed a mechanism for dynamic recrystallization inside the ASBs based on dislocations dynamics. They suggest that during high speed deformation, grains elongate into substructures, and the elongated substructures break into subgrains, resulting in recrystallized grains. In this study, rotational dynamic recrystallization happened same as Xu's work.

4. Mathematical modeling

Two constitutive equations were used for describing the response of the investigated MS to high strain-rate torsional deformation. One of these equations is an empirical model (Kobayashi and Odd (Kobayashi and Dodd, 1989) (Lee et al., 2004)), and the other one is a physically-based model which incorporates dislocation interaction (Nemat-Nasser and Isaacs model (Nemat-Nasser and Isaacs, 1997)).

4.1. Kobayashi-Odd model

Based on the available experimental data, the dependence of true shear stress on true shear strain under dynamic loading of MS was determined based on the equation suggested by Kobayashi and Odd (Kobayashi and Dodd, 1989) (Lee et al., 2004). Plastic region of the shear strain-shear stress curves can be described based on equation (10):

$$\tau = B.\gamma^{n}\gamma'^{m}(1 - \mathrm{CT}) \tag{10}$$

where n, m, B, and C are material unchanging parameters and are listed in Table 4. The term B. $\gamma^{n}\gamma'^{m}$ represents a power law of strain rate hardening albeit the term $(1 - \mathrm{CT})$ represent strain softening. In this equation, the temperature can be calculated based on equation (7).

The correlation between experimental data and model predicting the response of the twisted MS samples is shown in Fig. 13. It may be concluded that the model is compatible with the experimental data.

4.2. Nemat Nasser-Isaacs model

In this model, which is an example of a thermal activation model, stress is decomposed in long-range barriers that cannot be defeated by thermal energy and short-range barriers which can be assisted by thermal energy. In this model, the concept of dislocation motion during plastic deformation is used for describing the flow stress. For MS with BCC structure, the Peierls barriers (short-range barriers) are the only barriers to dislocation motion. Nemat- Nasser proposed the following equation to estimate dynamic deformation with regard to temperature, strain rate, and strain (Nemat-Nasser and Isaacs, 1997):

$$\tau = \tau 0.\gamma^{n} + \tau\hat{}(1 - \{-\left(\frac{k}{G0}\right)T(\ln(\frac{\gamma'}{\gamma'^{r}}) + \ln(\frac{\gamma''}{\gamma'})\}^{1/q})^{1/q} \tag{11}$$

where $\hat{\tau}$ is the threshold stress of Peierls barrier to dislocation motion, G_0 is the equivalent energy and K is the Boltzmann constant. G_0 is considered as 1 ev/atom then

Table 4
Determined parameters values of Kobayashi-Odd model.

Sample	B (MPa.s)	C(K^{-1})	n	m
3°	1200	0.00001	0.5	0.002
6°	800	0.00001	0.25	0.05
9°	630	0.00045	0.45	0.2
12°	330	0.0029	0.8	0.7

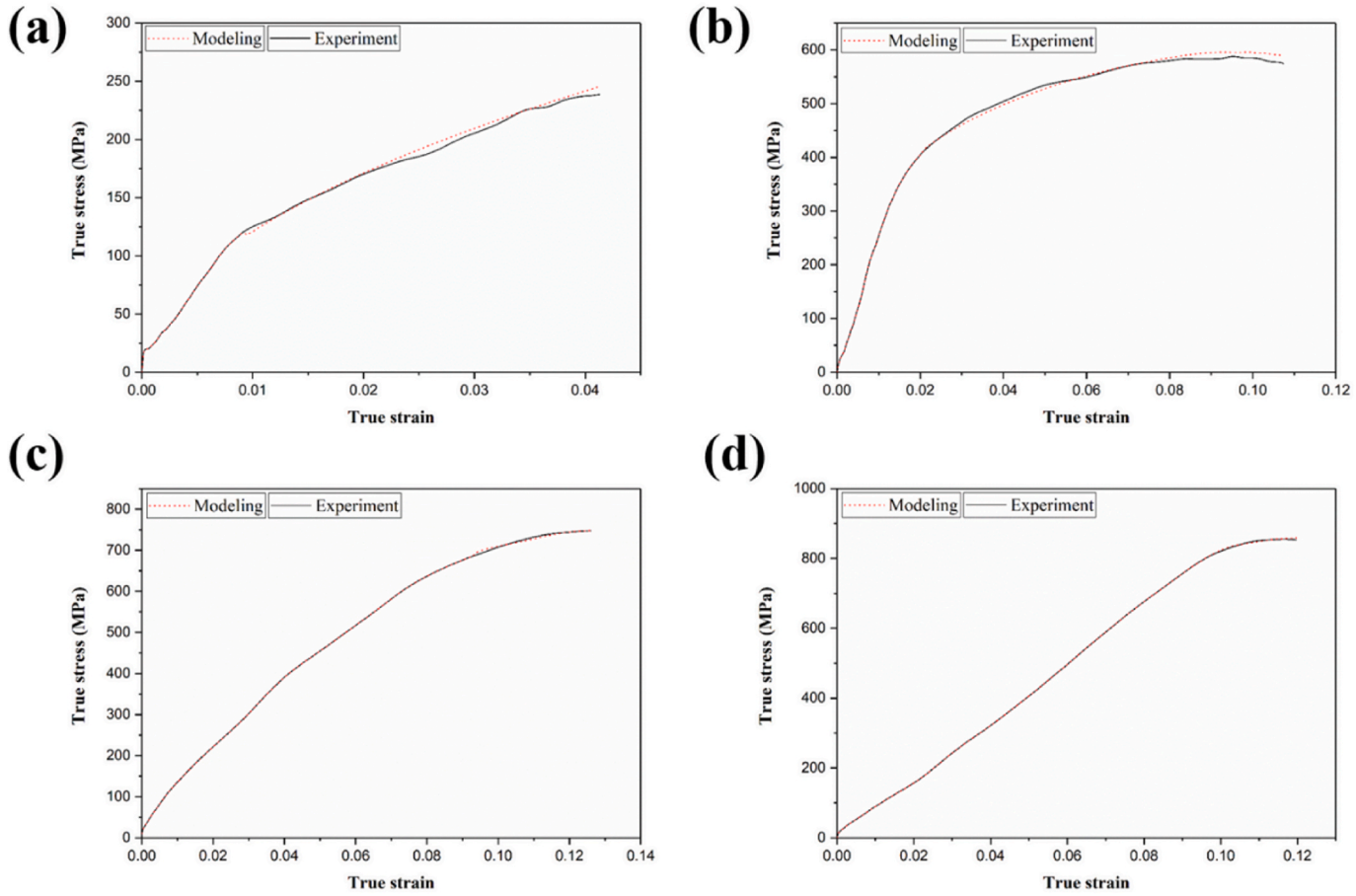

Fig. 13. Correlation of the tested flow stress curves and the Kobayashi-Odd model description for (a) 3°-260 s^{-1}, (b) 6°-650 s^{-1}, (c) 9°-720 s^{-1}, (d) 12°-650 s^{-1}.

$$\frac{k}{G0} = 8.62*10^{-5}K^{-1} \tag{12}$$

γ'^{r} is the reference strain rate, which is calculated by equation (13) with regard to Burgers vector and density of dislocations:

$$\gamma'^{r} = \rho b^2 w0 \tag{13}$$

where w_0 is the attempt frequency and Kocks considered it as 10^{12} s^{-1} (Kocks, 2001). The burgers vector magnitude for MS is taken as 0.249 nm (Dehgahi et al., 2021c), and the dislocation density in MS before plastic deformation is taken as 10^{15} m^{-2} (Dehgahi et al., 2020). With these assumptions, the reference strain rate is obtained as

$$\gamma'^{r} = 6.2 * 10^{7} s^{-1} \tag{14}$$

In equation (11), the temperature can be calculated based on equation (7) by considering that plastic work is transformed to heat. In this equation, q and p are unchanging factors that describe the profile of the energy barrier and are suggested by Kocks (2001).

In this equation, $\boldsymbol{\tau 0}.\gamma^{n}$ is taken as athermal component of the flow stress and the rest of equation is considered thermally activated component of flow stress. Table 5 shows the parameters of Nemat Nasser-Isaacs equation.

Table 5
Calculated parameters values of Nemat-Nasser model.

Sample	τ0 (MPa)	$\dot{\tau}$(MPa)	n	q	p
3°	1200	300	0.5	1.5	0.1
6°	1000	350	0.35	1.5	0.5
9°	1330	450	0.3	1	0.1
12°	905	500	0.17	2	0.66

Fig. 14 compares the results of the Nemat-Nasser model with experimental data in which the fit is acceptable. As shown in Fig. 15, with an increase in the angle of twist, the $\dot{\tau}$ values have increased ascribable to dislocation density increment; alternatively n values, which are indicative of work hardening, have been reduced with angle of twist enhancement ascribable to the superiority of thermal softening over strain-hardening.

5. Conclusions

The high speed performance of LPBF-MS in torsion has been studied using SHTB apparatus. With the change of angle of twist in the SHTB apparatus, different strain rates were generated in the thin-walled tubular test specimens. In the torsion test specimens, the applied angle of twist of 3, 6, 9, and 12° generated strain rates of 260, 650, 720 and 650 s^{-1}, respectively. Due to the small wall thickness of the torsion specimen, the shear strain rate, shear strain, and temperature are assumed to be localized in this part of the specimen. The MS fractured when the applied twist angle was increased to 12° (strain rates of 650 s^{-1}). Microstructural and textural analyses were done on twisted samples, and results showed that shear localization and ASBs are responsible for the fracture of the twisted sample. Texture intensity is reduced with an increment in strain rate ascribable to grain fragmentation at high speeds. Furthermore, the Kobayashi–Odd and Nemat-Nasser constitutive models were successfully developed to describe the dynamic shear stress-strain response of LPBF-MS.

Author contribution

Shirin Dehgahi: Conducting experiment, Numerical modeling, and

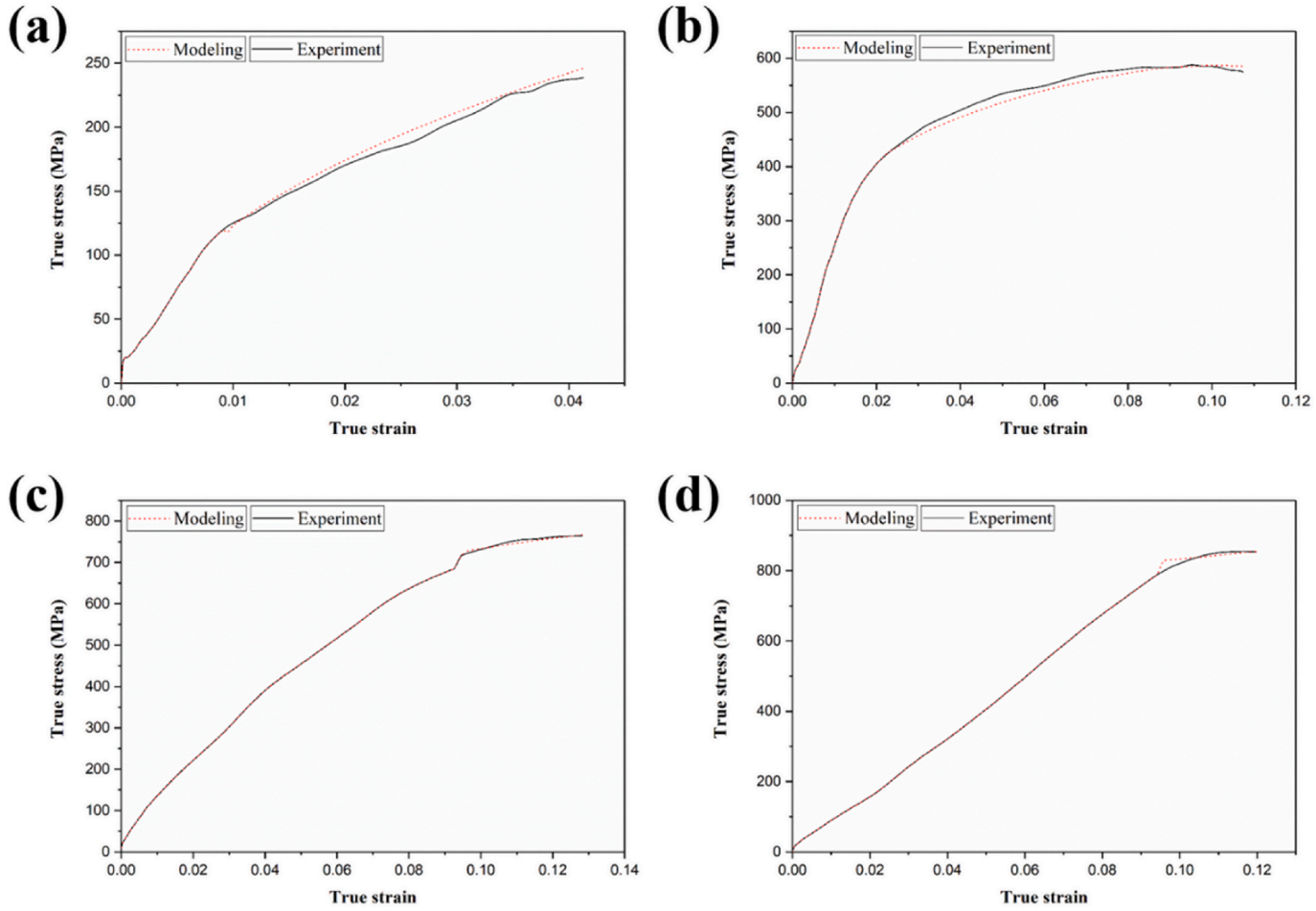

Fig. 14. Correlation of the tested flow stress curves and the Nemat-Nasser model description for (a) 3°-260 s^{-1}, (b) 6°-650 s^{-1}, (c) 9°-720 s^{-1}, (d) 12°-650 s^{-1}.

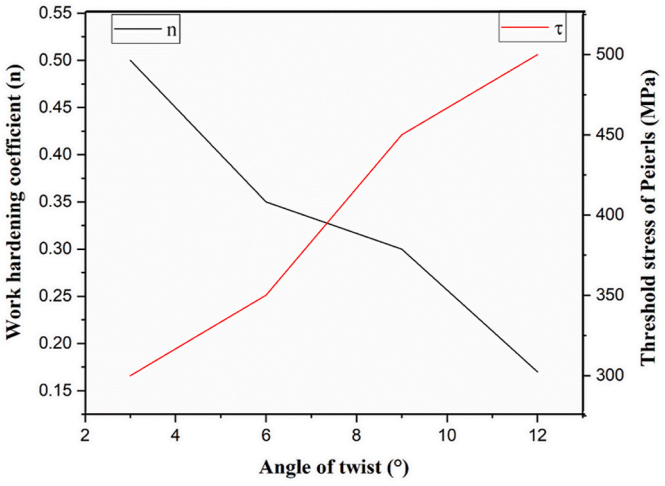

Fig. 15. Threshold stress of Peierls stress and work hardening coefficient as a function of angle of twist.

validation, writing the original draft. • Hadi Pirgazi: Conducting EBSD analysis & Writing - review & editing. Mehdi Sanjari: Writing - review & editing. Payam Seraj: Numerical modeling and validation & Writing - review & editing. Akindele Odeshi: Conducting Split Hopkinson torsion bar test, Writing - review & editing. Leo Kestens: Writing - review & editing. Mohsen Mohammadi: Funding acquisition, Project administration, Supervision.

Declaration of competing interest

The authors declare that they have no known competing financial interests or personal relationships that could have appeared to influence the work reported in this paper.

Acknowledgments

The funding from Atlantic Canada Opportunities Agency (ACOA)-Atlantic Innovation Fund (AIF) project number 210414 and Mitacs Accelerate Program grant number IT10669 are acknowledged. The help from Additive Metal Manufacturing (AMM) in Concord, Ontario, for fabricating the samples is much appreciated.

References

Alaghmandfard, R., Dharmendra, C., Odeshi, A.G., Mohammadi, M., 2020. Dynamic mechanical properties and failure characteristics of electron beam melted Ti-6Al-4V under high strain rate impact loadings. Mater. Sci. Eng. 793, 139794.

Baczynski, J., Jonas, J.J., 1996. Texture development during the torsion testing of α-iron and two IF steels. Acta Mater. 44, 4273–4288.

Baker, W.E., Yew, C.H., 1966. Strain-rate Effects in the Propagation of Torsional Plastic Waves.

Canova, G.R., Fressengeas, C., Molinari, A., Kocks, U.F., 1988. Effect of rate sensitivity on slip system activity and lattice rotation. Acta Metall. 36, 1961–1970.

Chen, G., Li, L.T., Qiao, J.W., Jiao, Z.M., Ma, S.G., Ng, F.L., Zhu, Z.G., Zhao, D., Wang, Z. H., 2019. Gradient hierarchical grain structures of Al0. 1CoCrFeNi high-entropy alloys through dynamic torsion. Mater. Lett. 238, 163–166.

Conde, F.F., Escobar, J.D., Oliveira, J.P., Béreš, M., Jardini, A.L., Bose, W.W., Avila, J.A., 2019. Effect of thermal cycling and aging stages on the microstructure and bending strength of a selective laser melted 300-grade maraging steel. Mater. Sci. Eng. 758, 192–201.

de Souza, A.F., Al-Rubaie, K.S., Marques, S., Zluhan, B., Santos, E.C., 2019. Effect of laser speed, layer thickness, and part position on the mechanical properties of maraging 300 parts manufactured by selective laser melting. Mater. Sci. Eng. 767, 138425.
Dehgahi, S., Ghoncheh, M.H., Hadadzadeh, A., Sanjari, M., Amirkhiz, B.S., Mohammadi, M., 2020. The role of titanium on the microstructure and mechanical properties of additively manufactured C300 maraging steels. Mater. Des. 108965.
Dehgahi, S., Alaghmandfard, R., Tallon, J., Odeshi, A., Mohammadi, M., 2021a. Microstructural evolution and high strain rate compressive behavior of as-built and heat-treated additively manufactured maraging steels. Mater. Sci. Eng. 815, 141183.
Dehgahi, S., Pirgazi, H., Sanjari, M., Alaghmandfard, R., Tallon, J., Odeshi, A., Kestens, L., Mohammadi, M., 2021b. Texture evolution during high strain-rate compressive loading of maraging steels produced by laser powder bed fusion. Mater. Char. 111266.
Dehgahi, S., Sanjari, M., Ghoncheh, M.H., Amirkhiz, B.S., Mohammadi, M., 2021c. Concurrent improvement of strength and ductility in heat-treated C300 maraging steels produced by laser powder bed fusion technique. Addit. Manuf. 101847.
Duffy, J., Chi, Y.C., 1992. On the measurement of local strain and temperature during the formation of adiabatic shear bands. Mater. Sci. Eng. 157, 195–210.
Gilat, A., Cheng, C.-S., 2000. Torsional split Hopkinson bar tests at strain rates above 10 4 s− 1. Exp. Mech. 40, 54–59.
Guduru, P.R., Rosakis, A.J., Ravichandran, G., 2001. Dynamic shear bands: an investigation using high speed optical and infrared diagnostics. Mech. Mater. 33, 371–402.
Gurao, N.P., Kapoor, R., Suwas, S., 2010. Effect of strain rate on evolution of the deformation microstructure and texture in polycrystalline copper and nickel. Metall. Mater. Trans. 41, 2794–2804.
Hadadzadeh, A., Baxter, C., Amirkhiz, B.S., Mohammadi, M., 2018a. Strengthening mechanisms in direct metal laser sintered AlSi10Mg: comparison between virgin and recycled powders. Addit. Manuf. 23, 108–120.
Hadadzadeh, A., Amirkhiz, B.S., Li, J., Odeshi, A., Mohammadi, M., 2018b. Deformation mechanism during dynamic loading of an additively manufactured AlSi10Mg_200C. Mater. Sci. Eng. 722, 263–268.
Khosravifard, A., Moshksar, M.M., Ebrahimi, R., 2013. High strain rate torsional testing of a high manganese steel: design and simulation. Mater. Des. 52, 495–503.
Kobayashi, H., Dodd, B., 1989. A numerical analysis for the formation of adiabatic shear bands including void nucleation and growth. Int. J. Impact Eng. 8, 1–13.
Kocks, U.F., 2001. Realistic constitutive relations for metal plasticity. Mater. Sci. Eng. 317, 181–187.
Kolsky, H., 1949. An investigation of the mechanical properties of materials at very high rates of loading. Proc. Phys. Soc. B 62, 676.
Lee, W.-S., Cheng, J.-I., Lin, C.-F., 2004. Deformation and failure response of 304L stainless steel SMAW joint under dynamic shear loading. Mater. Sci. Eng. 381, 206–215.
Majzoobi, G.H., Rahmani, K., Lahmi, S., 2019. Determination of length to diameter ratio of the bars in torsional Split Hopkinson bar. Measurement 143, 144–154.
Nemat-Nasser, S., Isaacs, J.B., 1997. Direct measurement of isothermal flow stress of metals at elevated temperatures and high strain rates with application to Ta and TaW alloys. Acta Mater. 45, 907–919.
Niu, Q., Ming, W., Chen, M., Tang, S., Li, P., 2017. Dynamic mechanical behavior of ultra-high strength steel 30CrMnSiNi2A at high strain rates and elevated temperatures. J. Iron Steel Res. Int. 24, 724–729.
Oliveira, J.P., LaLonde, A.D., Ma, J., 2020. Processing parameters in laser powder bed fusion metal additive manufacturing. Mater. Des. 193, 108762.
Shamsdini, S., Ghoncheh, M.H., Sanjari, M., Pirgazi, H., Amirkhiz, B.S., Kestens, L., Mohammadi, M., 2020. Plastic deformation throughout strain-induced phase transformation in additively manufactured maraging steels. Mater. Des. 198, 109289.
Shen, Y.F., Jia, N., Misra, R.D.K., Zuo, L., 2016. Softening behavior by excessive twinning and adiabatic heating at high strain rate in a Fe–20Mn–0.6 C TWIP steel. Acta Mater. 103, 229–242.
Sing, S.L., Yeong, W.Y., 2020. Laser powder bed fusion for metal additive manufacturing: perspectives on recent developments. Virtual Phys. Prototyp. 15, 359–370.
Tiamiyu, A.A., Odeshi, A.G., Szpunar, J.A., 2018. Multiple strengthening sources and adiabatic shear banding during high strain-rate deformation of AISI 321 austenitic stainless steel: effects of grain size and strain rate. Mater. Sci. Eng. 711, 233–249.
Tian, C., Ponge, D., Christiansen, L., Kirchlechner, C., 2020. On the mechanical heterogeneity in dual phase steel grades: activation of slip systems and deformation of martensite in DP800. Acta Mater. 183, 274–284.
Tiwari, S., Mishra, S., Odeshi, A., Szpunar, J.A., Chopkar, M., 2017. Evolution of texture and microstructure during high strain rate torsion of aluminium zinc magnesium copper alloy. Mater. Sci. Eng. 683, 94–102.
Xu, Y., Zhang, J., Bai, Y., Meyers, M.A., 2008a. Shear localization in dynamic deformation: microstructural evolution. Metall. Mater. Trans. 39, 811–843.
Xu, Y., Yang, H.J., Meyers, M.A., 2008b. Dynamic recrystallization in the shear bands of Fe–Cr–Ni monocrystal: electron backscatter diffraction characterization. Scripta Mater. 58, 691–694.
Zhou, M., Rosakis, A.J., Ravichandran, G., 1996. Dynamically propagating shear bands in impact-loaded prenotched plates—I. Experimental investigations of temperature signatures and propagation speed. J. Mech. Phys. Solid. 44, 981–1006.